

# Design and demonstrators testing of adaptive airfoils and hingeless wings actuated by shape memory alloy wires

Giuseppe Mirone<sup>†</sup>

*Dipartimento di Ingegneria Industriale e Meccanica, University of Catania, Viale Andrea Doria 19, 95125 - Catania, Italy*

*(Received May 24, 2005, Accepted June 7, 2006)*

**Abstract.** Two aspects of the design of a small-scale smart wing are addressed in this work, related to the ability of the wing to modify its cross section assuming the shape of two different airfoils and to the possibility of deflecting the profiles near the trailing edge in order to obtain hingeless control surfaces. The actuation is provided by one-way shape memory alloy wires eventually coupled to springs, Shape Memory Alloys (SMAs) being among the most promising materials for this kind of applications. The points to be actuated along the profiles and the displacements to be imposed are selected so that they satisfactorily approximate the change from an airfoil to the other and to result in an adequate deflection of the control surface; the actuators and their performances are designed so that an adequate wing stiffness is guaranteed, in order to prevent excessive deformations and undesired airfoil shape variations due to aerodynamic loads. The effect of the pressure distributions, calculated by way of the XFOIL software, and of the actuators loads, is estimated by FE analyses of the loaded wing. Two prototypes are then realised incorporating the variable airfoil and the hingeless aileron features respectively, and the verification of their shapes in both the actuated and non-actuated states, supported by image analysis techniques, confirms that interesting results are achievable with the proposed lay out and design considerations.

**Keywords:** Shape Memory Alloy; adaptive wing; hingeless wing; SMA actuator; compliant structure; finite element method; image analysis.

---

## 1. Introduction

A very promising way to optimise a wing for more than a single flight condition is to make its section capable of assuming different airfoil shapes, each specifically tailored for one of the selected air flow regimes (Strelec, *et al.* 2003, Garner, *et al.* 2000).

Another desirable feature, able to increase the overall efficiency of a wing, is the absence of hinges and other discontinuities which usually characterize the boundaries between the main lift-generating surfaces and the control surfaces (Monner 2001).

Both these issues are achievable by imposing controlled smooth deformations to compliant hingeless profiles (Lu and Kota 2002) and the choice of shape memory alloy wires, rods or beams, as mean of actuation and control of the profiles deformation, is largely justified by the small dimensions and the considerable work per unit mass these SMA components are capable of (Elzey, *et al.* 2005, Icardi 2001,

---

<sup>†</sup>Researcher, E-mail: [gmirone@diim.unict.it](mailto:gmirone@diim.unict.it)

Huang 2002).

The present paper regards the implementation of the aforementioned smart features on the wing of an unmanned air vehicle (Neal, *et al.* 2004) with a wingspan included in the range 1-5 m, typical of many short-range Unmanned Air Vehicles (UAVs, Van Blyenburgh 1999).

The experimental characterization of the SMA used for this work is performed by way of the typical temperature-strain cycles at constant load and stress-strain cycles at constant temperature (Brinson, *et al.* 1996, Trochu, *et al.* 1999).

The “reflex” airfoils Eppler E328 and Eppler E329, suitable for tailless plane configurations due to their self-stabilizing pitching attitude (Di Lecce 1977, Kroo 1997, Talay 1975), are selected as the shapes to be imposed to the wing cross section in the unactivated and activated configurations respectively. The choice of these two profiles is mainly due to an appreciable difference between their thickness, but the variable airfoil concept obviously applies also to profile couples selected on the basis of more specific aerodynamic considerations.

Finite Elements (F.E.) analyses are performed to help in deciding which points are to be displaced and which forces are needed to approximate the desired profiles transformations.

According to the demonstrative character of this paper, the profile variation is accomplished only on the upper half of each airfoil, but, for the estimation of the aerodynamic actions, the complete profiles are considered.

The actuators are based on one-way Nickel-Titanium (NiTi) wires, coupled to springs in order to force them to elongate in the martensitic state, which corresponds to the unactivated configuration of the wing (E 328 airfoil); when the wires are heated by the Joule effect, they overcome the resisting force of the springs and the elastic reaction of the wing, contracting themselves until the final configuration is assumed (E 329 airfoil).

The NiTi actuators are designed to work in the fully austenitic and fully martensitic phases, so that intermediate compositions are to be considered as only transitory and of no interest in the present work. This allows to model the SMA behaviour with a much simpler approach than that of many models in which a continuous temperature-stress-strain dependence is described (Brinson 1993, Tanaka, *et al.* 1995, Auricchio, *et al.* 1997, Lu, *et al.* 1997, Govindjee, *et al.* 2000, Brocca, *et al.* 2002).

A prototype of the adaptive upper half wing is then realized and tested with regard to its ability in approximating the Eppler airfoils depending on the activation current which feeds the SMA wires.

Image analysis techniques are used to measure the coordinates of many points on the wing profiles (Flemings, *et al.* 1999) in both the active and unactivated states, allowing a successive comparison with the coordinates of the ideal profiles.

A similar procedure is carried out for the study of the hingeless control surface, passing through the F.E. calculation of the required force and wire contraction, the calculation of the necessary wire length, the construction and testing of a concept demonstrator.

## 2. Adaptive airfoil lay out

The E328 and E329 airfoils, scaled for a 500 mm chord, are represented in Fig. 1 where the vertical axis is stretched in order to evidence the thickness differences.

This work is focused on modifications of the wing shape in its transverse plane, thus the spanwise aspects of the platform (wing tapering, sweep, dihedral or twist) are not analysed; the wing structure module of our interest is depicted in the scheme of Fig. 2 as the part covered by a transparent skin.

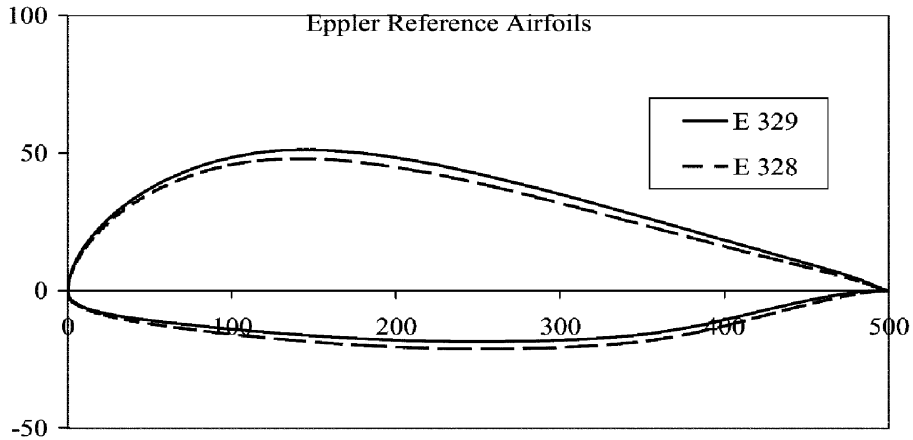


Fig. 1 500 mm chord reference airfoils

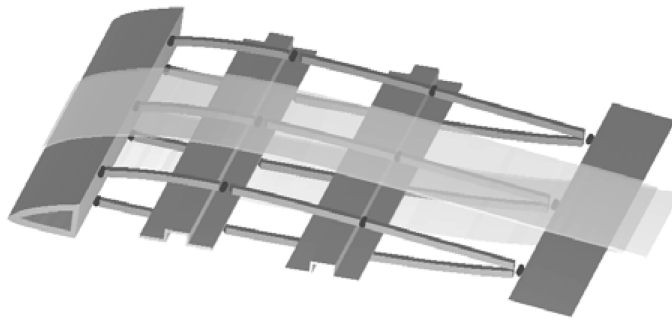


Fig. 2 Wing structural pattern

Each rib is thought to be constituted by closed-loop hinged elements, so that controlling the position of joints allows to approximate different airfoils. The center spars support the SMA actuators devoted to the joints motion.

Two joints are used to operate the upper surface of the wing structural pattern which is the subject of this work, although a greater number of joints (their number could be a variable in an optimization process) allows to better approximate the target airfoil E329 by deforming the initially undeformed E328.

The upper surface in the E329 airfoil is slightly longer than in the E328, thus a profile transformation made at constant chord value is possible only if the wing skin is able to stretch considerably; the other option, adopted in this work, is to maintain the same skin length and let the chord able to slightly contract itself during the profile transformation;

In order to choose the most favourable points to be actuated along the upper half of the E328 profile, the actuation work and the deformed shapes corresponding to different chordwise positions of the actuated joints are calculated by finite elements analyses, according to the load schemes in Fig. 3 (black arrows for the first actuator, white for the second);

the entire chord length  $C$  is scanned at steps of  $0.1C$  length, except for the neighbors of the trailing edge, where not enough space is available for the placement of the actuators.

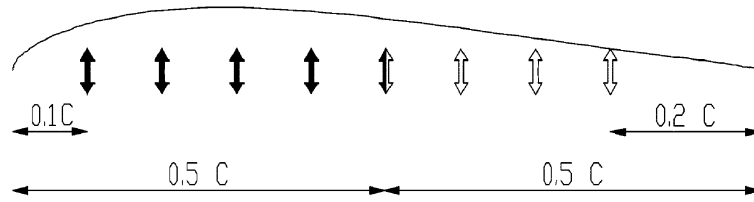


Fig. 3 Actuator positions evaluated

### 3. Identification of the actuator loads

In all the twenty F.E. models analysed with the “MARC” code, the ribs and the skin are modeled by hex 8 bricks and by quad 4 shells 0.7 mm thick respectively, the corresponding material elastic constants being those typical of hard wood and steel.

The structures are constrained on the leading edge nodes (all translational degrees of freedom locked) and of the trailing edge, (spanwise translations and vertical translations locked, chordwise translations permitted); each actuator load is modeled with an arbitrary vertical load distributed on the four nodes corresponding to a single rib joint (Fig. 4).

Every structure is analysed under two different loadcases, each corresponding to an arbitrary 100 N load for the first and the second actuator,  $L_{1\_100}$  and  $L_{2\_100}$  respectively.

The Principle of Effect Superposition, to which our structure is supposed to obey, allows us to calculate the load values  $L_1$  and  $L_2$ , required to the actuators in order to approximate the E329 target airfoil, according to the following description;

Let's  $PL_{1\_100}(x)$  and  $PL_{2\_100}(x)$  be best-fit polynomials of the two displacements fields which every F.E.A. gives after being run with the first and second loadcase, respectively;  $x_1$  and  $x_2$  are the chordwise abscissae corresponding to the first and second actuators; then we can find two scale factors,  $a_1$  and  $a_2$ , such that:

$$\begin{cases} a_1 \cdot PL_{1\_100}(x_1) + a_2 \cdot PL_{2\_100}(x_1) = E329(x_1) - E328(x_1) \\ a_1 \cdot PL_{1\_100}(x_2) + a_2 \cdot PL_{2\_100}(x_2) = E329(x_2) - E328(x_2) \end{cases} \quad (1)$$

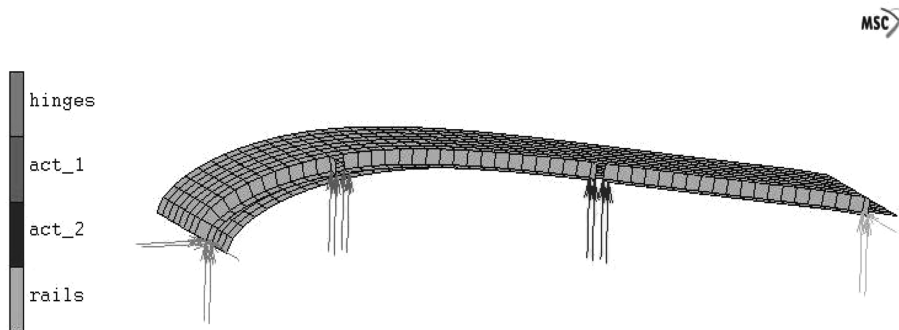


Fig. 4 Adaptive airfoil FE model

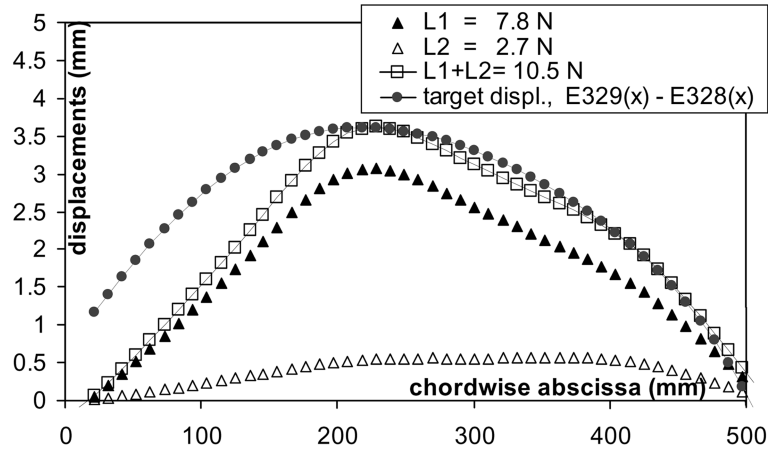


Fig. 5 Actuation displacements for the 200-400 configuration

where  $E328(x)$  and  $E329(x)$  are the best-fit 6<sup>th</sup> polynomials for the target airfoils. Once obtained from Eq. (1), the scaling parameters  $a_1$  and  $a_2$  are used to calculate the actuator loads  $L_1$  and  $L_2$  and the displacements field  $Def(x)$  expected when these loads are applied simultaneously:

$$\begin{aligned} L_1 &= a_1 \cdot L_{1\_100} \\ L_2 &= a_2 \cdot L_{2\_100} \\ Def(x) &= a_1 \cdot PL_{1\_100}(x) + a_2 \cdot PL_{2\_100}(x) \end{aligned} \quad (2)$$

In Fig. 5 is visible the comparison between the profile displacements for the 200-400 configuration, (first actuator placed 200 mm behind the leading edge, 2<sup>nd</sup> actuator 400 mm behind the leading edge) and the desired displacements given by  $E329(x) - E328(x)$ .

It is visible that, as imposed in Eq. (1), at the abscissae values where the actuators are placed, 200 and 400 mm, the induced total displacements are equal to those required to transform the Eppler 328 into the Eppler 329 (target displacements), but, at other locations along the chord, the activated profile differs from the target shape  $E329$ .

In some configurations among those tested, the required actuators loads resulted to have opposite signs as in Fig. 6, resulting in significant actuation energy and/or poor actuation efficiency: in these cases, one of the actuators (often the second one) is suppressed leaving un-actuated the corresponding rib joint; the resulting structure performance (Fig. 7) is very slightly decreased in terms of displacement accuracy, but greatly improved in terms of actuation efficiency.

Once the deformed shape and the corresponding loads are found for all the actuators configurations analysed, the activation work and a “profile discrepancy parameter” are calculated in Eq. (3) as tools for the performance evaluation of each configuration:

$$\begin{aligned} W &= \frac{1}{2}(L_1 \cdot Def(x_1) + L_2 \cdot Def(x_2)) \\ DP &= \sqrt{\int_0^c [E328(x) + Def(x) - E329(x)]^2 dx} \end{aligned} \quad (3)$$

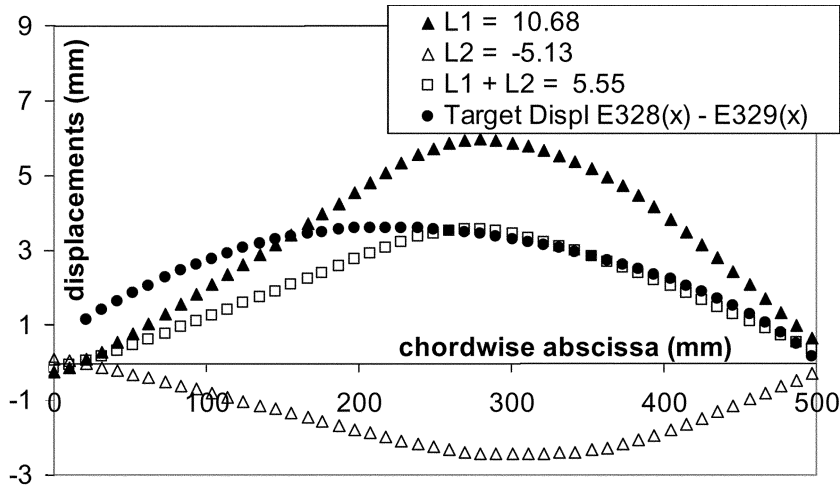


Fig. 6 Actuation displacements for the 250-350 configuration

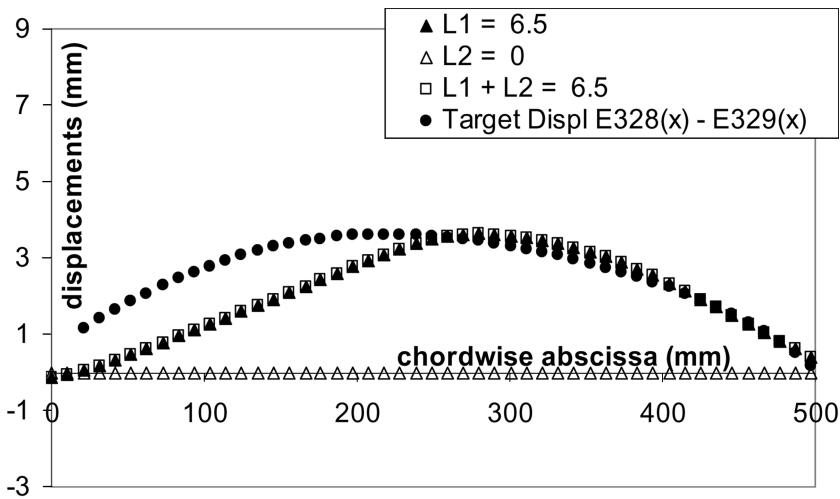


Fig. 7 Actuation displacements for the 250-350 configuration without 2nd actuator

The discrepancy parameter expresses the cumulative sum of absolute values of the gaps between the deformed E328 profile and the target E329 airfoil: the higher is  $DP$ , the worse does the actuators placement allow to reproduce the E329 airfoil.

In Figs. 8 and 9 are displayed the required activation energy values and the discrepancy parameters as functions of the actuators positions.

The energy values related to the wing configurations where the first actuator is placed too close to the leading edge (50 mm) are much greater than the others because high loads are required due to the significant stiffness in the areas of the skin with higher curvature.

The 250-250 case clearly refers to just one actuator placed 250 mm far from the leading edge.

The ideally most favourable case would be that of a configuration being at the same time the less energetically expensive to be activated and the more accurate in reproducing the E329 shape, but, for

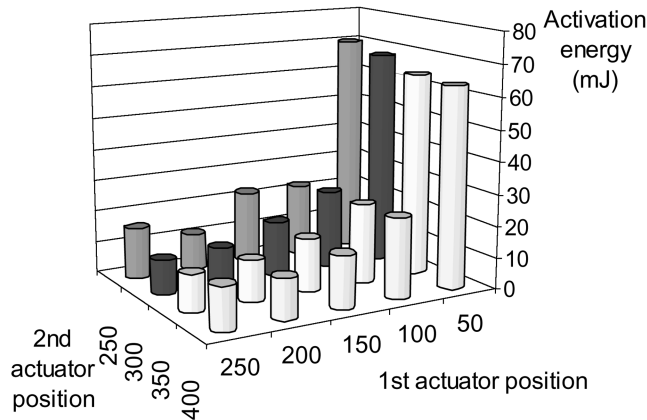


Fig. 8 Activation work as function of the actuators placement

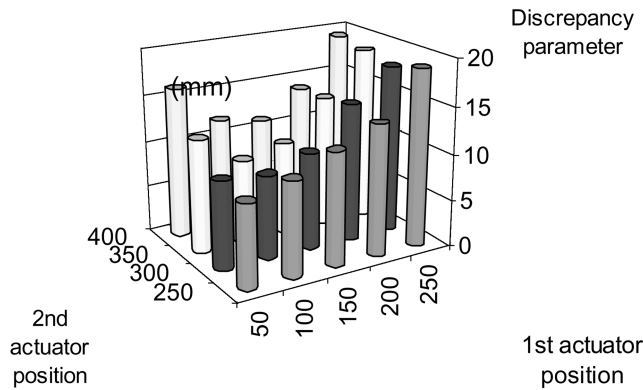


Fig. 9 Profile discrepancy function of the actuators placement

the finite discretization adopted, the better configurations in the two viewpoints are the 250-300 (1<sup>st</sup> actuator 250 mm and 2<sup>nd</sup> actuator 300 mm far from the leading edge, minimum required energy  $10.8 \times 10^{-3}$  J) and the 100-300 (1<sup>st</sup> actuator 100 mm and 2<sup>nd</sup> actuator 300 mm far from the leading edge, minimum discrepancy parameter equal to 9.03 mm) respectively.

In the latter configuration, the second actuator is not required to work as for the 250-350 structure; in these cases, the second number of the configuration name indicates just that a rib hinge is present at the chordwise abscissa specified.

The model 100-300 is the more performing in the whole lot with regard to the shape accuracy, and is selected for further investigations and prototype development because its activation energy of  $24.8 \times 10^{-3}$  J, tough not being the minimal, is largely compatible with the performance of the typical SMA wires to be used for the actuators.

The comparison between the displacement field ideally needed to transform the E328 in the E329 airfoil and the best displacement field induced by a single actuator placed 100 mm behind the leading edge, is reported in Fig. 10.

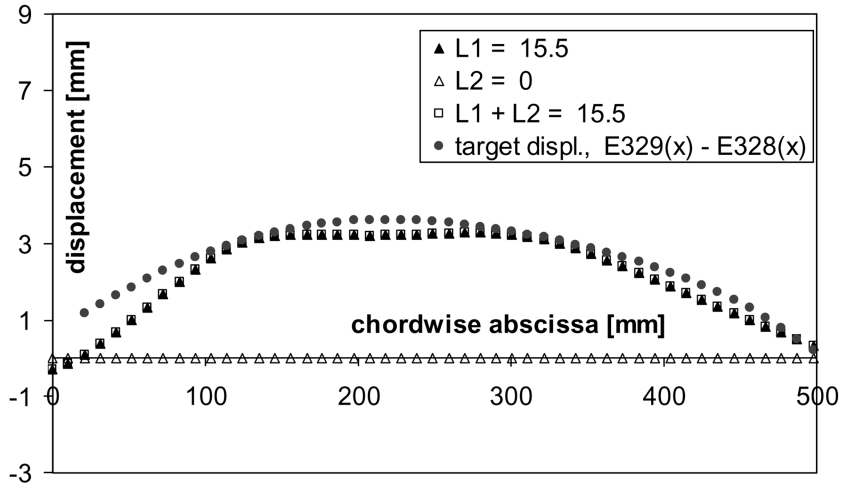


Fig. 10 Actuation displacements for the 100-300 configuration without 2nd actuator

#### 4. SMA characterization

The used SMA is available in the form of 1.25 mm diameter NiTi wires, for which the first series of experimental tests are performed in order to determine the transformation temperatures. The wires are loaded at a constant level and their temperature, measured in real-time with an infra-red imagery system Agema Thermovision 470 is varied by controlling the direct current feeding; the temperature is varied cyclically at fixed steps, and the wire length is measured at each step by means of image analysis techniques. The resulting strain-temperature curves, evaluated at the three constant-stress values of 20, 40 and 55 MPa, show the typical hysteretic shapes of Fig. 11.

The same test, performed at stress levels above 60 MPa, produced permanent deformations at lower temperatures.

The successive series of experimental tests was made to determine the stress-strain curves at six temperature values between 15 and 120 °C, as reported in Fig. 12.

The maximum “shape memory” strain, to be imposed in the martensitic phase and recovered in the austenitic one, was verified to be close to 6%.

The  $M_f$  temperature below which the SMA is in its fully martensitic phase, regardless of the applied stress, lies between 15 and 20 °C, while the fully austenitic phase exists only for opportune combinations of temperature and stress: for stress values up to 400 MPa, a temperature of 120 °C ensures that the SMA is fully austenitic.

The unloading path in the stress-strain curves is not recorded because, for our application, unloading of any structure is only a consequence of the austenite-martensite transformation, and no load reduction is allowed without the latter transformation.

The stress-strain curves at 40 and 60 °C show that the saturation of the stress-induced Martensite, at 200 MPa and 300 MPa, causes the elastic modulus to increase returning close to the values of the fully austenitic phase.

The transformation temperatures are then expressed as functions of the applied stress as in Fig. 13: The low value of the  $M_f$  temperature implies that the room temperature may not be compatible with

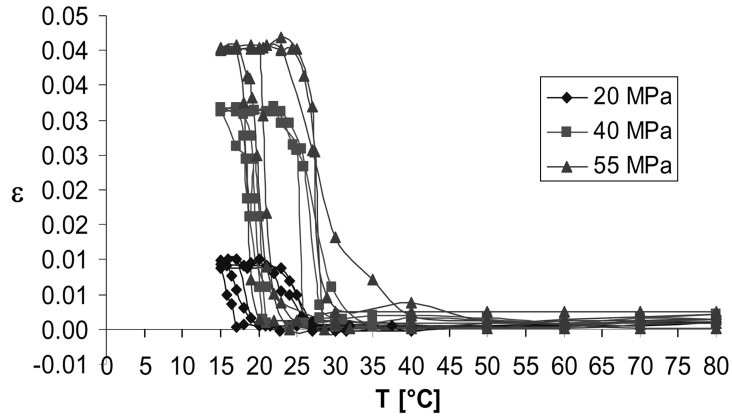


Fig. 11 Strain vs. temperature hysteresis cycles at three load levels

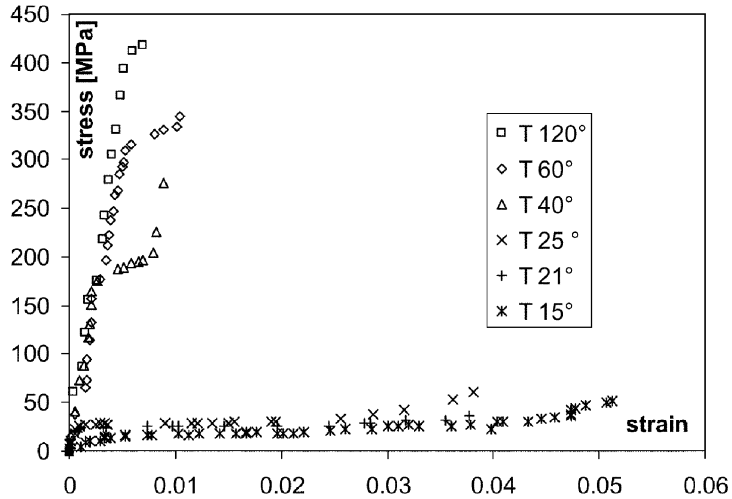


Fig. 12 Stress-strain curves at different temperatures

the fully martensitic state, but, in the generality of our viewpoint, the temperature of the air surrounding the wing in flight is supposed to be lower than  $M_f$ .

These experimental data, together with the structural requirements and constraints derived from the analysis of the wing section, are the basis for the design of the actuators.

### 5. Actuators modeling

The basic actuator specifications obtained so far can be summarised as in Table 1:

Table 1 Actuation parameters

Actuator	Displ. [mm]	Force [N]	Work [ $J \times 10^{-5}$ ]
#1	3.02	18	27.4

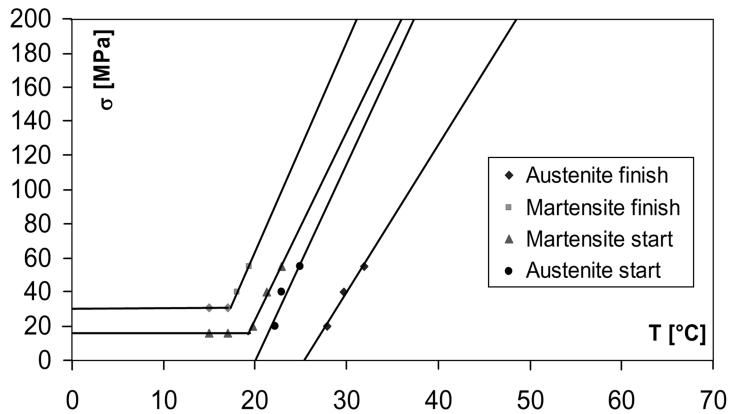


Fig. 13 Transformation temperatures vs. applied stress

The needed displacements would require SMA lengths above 60 mm, assuming that the entire 5% recoverable strain range is used to produce the actuation work; this length value is close to the airfoil thickness, thus, in order to place the actuators into the profile perimeter, these may only be placed parallel to the chord direction where more room is available. The actuator lay-out of Fig. 14 is chosen for successive development.

As mentioned previously, the presence of a spring within the actuator assembling is needed for two reasons; the first is that the one-way SMA wires are to be stretched by an external force when, at low temperatures, the E328 profile shape is to be set, (the elastic reaction of the structure could not be able to elongate the SMA in its “cold” state); the second reason is that the spring constitutes the straighter way to give the wing section an adequate stiffness in the transverse plane, preventing excessive airfoil deformations due to the airflow pressure in the E328 or E329 settings.

Then, though the second actuator is not essential for the profile shape transformation of the E328 in the E329 airfoil, its presence is required to increase the value of the wing section stiffness.

Once the SMA properties are fixed in terms of stress – strain – temperature relationships, the actuators design variables are the following ones:

- $l$ , undeformed free length of the SMA wire;
- $d$ , SMA wire diameter;
- $K$ , spring stiffness;

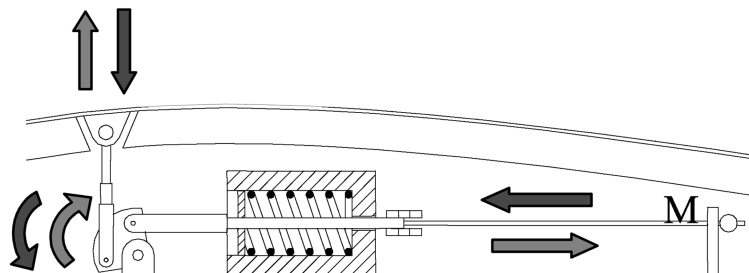


Fig. 14 Actuators layout

- $\Delta l_0$ , spring-wire preload displacement;

The actuator output variables, corresponding to the two extreme states of a full phase transformation, for each given set of the above parameters are:

- $\Delta l_A$ , austenite elongation;
- $F_A$ , austenite load;
- $\Delta l_M$ , martensite elongation;
- $F_M$ , martensite load;

The first step in modelling the actuator is to write the load-displacement laws for an initially undeformed SMA wire of diameter  $d$  and length  $l$ , in the austenitic and martensitic phases; if  $\sigma_A(\varepsilon)$  and  $\sigma_M(\varepsilon)$  are the best-fit polynomials describing the experimental stress-strain curves at 120 °C and 25 °C, linear and 3<sup>rd</sup> order respectively, then:

$$F_A(\Delta l) = \sigma_A\left(\frac{\Delta l}{l}\right) \cdot \frac{\pi}{4} \cdot d^2$$

$$F_M(\Delta l) = \sigma_M\left(\frac{\Delta l}{l}\right) \cdot \frac{\pi}{4} \cdot d^2 \quad (4)$$

The SMA wire and the spring are initially assembled into the actuator at room temperature (below  $Mf_0$ ) so that, with the wire at its undeformed length  $l$  (after an heating cycle above  $Af$  without any constraint), the spring is not compressed at all and no clearance or gap is present in the assembling. Then, the adjustable end of the wire (point  $M$  in Fig. 14) is pulled backward of the quantity  $\Delta l_0$ ; this translation splits into two components, one ( $\Delta l_{SM}$ ) inducing a compressive pre-load of the spring and the other ( $\Delta l_M$ ) elongating the martensitic wire, so that  $\Delta l_{SM} + \Delta l_M = \Delta l_0$ . The spring-wire equilibrium equation in this condition is:

$$F_M(\Delta l_M) = \sigma_M\left(\frac{\Delta l_M}{l}\right) \cdot \frac{\pi}{4} \cdot d^2 = K \cdot (\Delta l_0 - \Delta l_M) \quad (5)$$

If the wire is heated, it starts to contract itself inducing further compression of the spring, whose increased elastic reaction opposes in turn the wire effort to entirely recover the  $\Delta l_M$  elongation returning to its original length  $l$ ;

When the wire temperature is equal or above  $Af$  its elongation is decreased from  $\Delta l_M$  down to the actual value  $\Delta l_A$  and the spring compression increases from  $\Delta l_0 - \Delta l_M$  up to  $\Delta l_0 - \Delta l_A$ , thus, for the equilibrium:

$$F_A(\Delta l_A) = \sigma_A\left(\frac{\Delta l_A}{l}\right) \cdot \frac{\pi}{4} \cdot d^2 = K \cdot (\Delta l_0 - \Delta l_A) \quad (6)$$

Temperature cycling above  $Af$  and below  $Mf$  will then induce cyclic movements of the actuator shaft with amplitude of  $\Delta l_M - \Delta l_A$ .

The considerations just made refers to the free actuator, but when it is placed “on duty” within the wing section, further resisting forces from the actuated structure and their dependence on the displacements are to be taken into account. In our case, these forces are the elastic reactions of the

deforming profiles previously analysed by F.E., and their effect may be introduced in Eqs. (5) and (6) in the form of a structure-induced increase of the spring stiffness; the global stiffness for each actuator is the sum of the contribution from the spring  $K$  and from the wing structure  $K'$ , because these are coupled as a parallel assembling of two springs. The pivoting L-shaped double lever shown in Fig. 11 has a kinematic reduction ratio of 1:1, thus the structure stiffness contributions are given by the simple ratio between the actuation loads and the corresponding profile displacements.

The structure-actuator model may be finally described by the following Eq. (7):

$$\begin{aligned}\sigma_A\left(\frac{\Delta l_A}{l}\right) \cdot \frac{\pi}{4} \cdot d^2 &= (K + K') \cdot (\Delta l_0 - \Delta l_A) \\ \sigma_M\left(\frac{\Delta l_M}{l}\right) \cdot \frac{\pi}{4} \cdot d^2 &= (K + K') \cdot (\Delta l_0 - \Delta l_M)\end{aligned}\quad (7)$$

If the model is completely identified by the SMA stress-strain curves and by the parameters  $l$ ,  $d$ ,  $K$ ,  $K'$ ,  $\Delta l_0$ , then Eq. (7) allows to calculate the  $\Delta l_M$  and  $\Delta l_A$  unknowns.

In our case,  $l$ ,  $K$  and  $\Delta l_0$  are unknowns to be determined by imposing three further mathematical constraints to the model equations, ensuring respectively that the actuator stroke changes the deforming structure among the desired airfoils shapes, that the wing-actuator structure is stiff enough to limit undesired profile shape modifications due to the aerodynamic pressure distributions, and that the maximum wire load in the austenitic phase does not exceed a maximum value  $F_{A_{Max}}$ ; the new set of equations is then:

$$\begin{aligned}\sigma_A\left(\frac{\Delta l_A}{l}\right) \cdot \frac{\pi}{4} \cdot d^2 &= (K + K') \cdot (\Delta l_0 - \Delta l_A) \\ \sigma_M\left(\frac{\Delta l_M}{l}\right) \cdot \frac{\pi}{4} \cdot d^2 &= (K + K') \cdot (\Delta l_0 - \Delta l_M) \\ \Delta l_M - \Delta l_A &= E329(X_{ACT}) - E328(X_{ACT}) \\ K + K' &= K_{REQ} \\ \sigma_A\left(\frac{\Delta l_A}{l}\right) \cdot \frac{\pi}{4} \cdot d^2 &= F_{A_{Max}}\end{aligned}\quad (8)$$

where  $K_{REQ}$  is the stiffness value required to prevent excessive aeroelastic deformations.

Eq. (8) allows to calculate the five unknowns  $\Delta l_A$ ,  $\Delta l_M$ ,  $l$ ,  $K$  and  $\Delta l_0$  from the knowledge of the functions  $\sigma_A(\varepsilon)$ ,  $\sigma_M(\varepsilon)$ ,  $E328(X)$ ,  $E329(X)$ , and of the parameters  $d$ ,  $K'$ ,  $F_{A_{Max}}$  and  $K_{REQ}$ .

The value of  $K_{REQ}$  to be input in Eq. (8) for each actuator, is derived from the application of an opportune pressure distribution all over the wing surface of an opportune F.E. model according to the description in the following section.

### 6. Determination of the actuator spring stiffenss

In order to determine the values of the actuators stiffness which are compatible with the aerodynamic loads and with acceptable values of the corresponding structure deformations, the airflow pressure distribution is evaluated for the E328 airfoil at a reference airflow regime; then this calculated pressure distribution is applied to a F.E. model derived from the 100-300 model previously analysed, with two elastic spring elements added in the positions occupied by the actuators arms.

The contribution of the actuators to the stiffness of the wing transverse section is due only to the springs, in fact the SMA wires would be compressed by the pressure-induced wing deformations, thus, in reality, they would buckle producing negligible axial reactions and negligible contribution to the wing stiffness.

The pressure distribution is calculated for the E328 airfoil because it is more prone than the E329 to large airflow-induced deflections; in fact, the former configuration lacks of the internal pre-tension due to the actuator loads which, on the contrary, helps the E329 to better withstand the airflow loads.

The pressure distribution shown in Fig. 15 is calculated by way of the “XFOIL” viscid-formulation

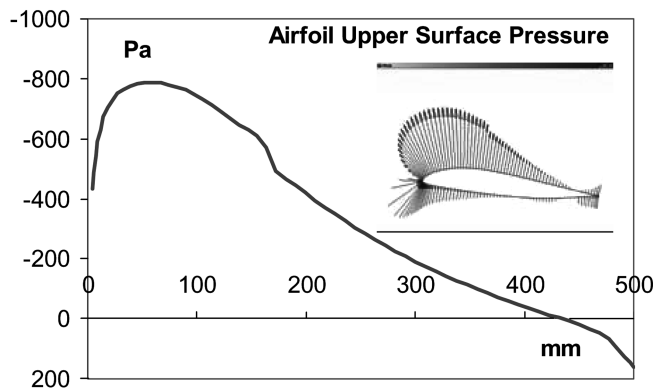


Fig. 15 Pressure distribution on E328 airfoil

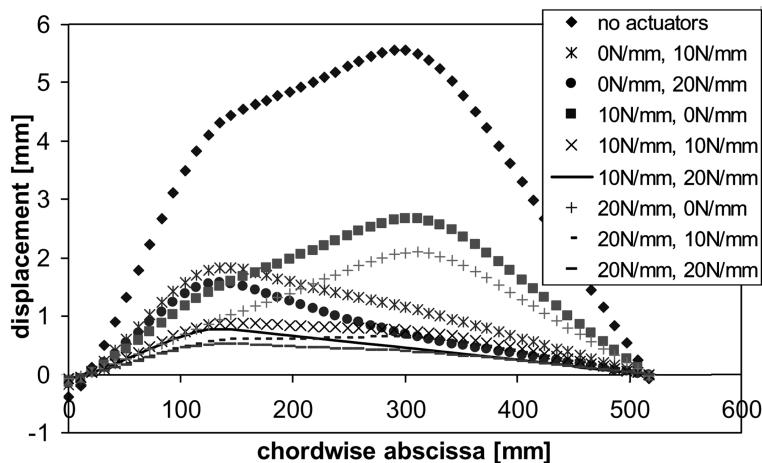


Fig. 16 Airflow-induced profile displacements for different combination of spring stiffensses

freeware code (Drela 2001) referring to an airspeed of 30 m/s, a  $Re$  number of  $1.02 \times 10^6$  and an incidence angle of 5 degs.

The stiffness values of the truss elements simulating the actuators springs are varied among the values of 0-10-20 N/mm, and the corresponding profile displacements due to the pressure distribution are summarised in Fig. 16. This analysis allows to select the appropriate values of the actuators' springs stiffness; their stiffness must be great enough to prevent excessive airfoil deformations but, at the same time, the higher is the springs stiffness, the higher becomes the load and the work required to the SMA wires.

Among the analysed combinations of springs stiffness values, that with 10 N/mm and 20 N/mm for the first and second actuator respectively is selected as a good compromise between the resulting transverse stiffness of the wing and the surplus of load-work required to the SMA wires due to the presence of the springs.

Two coil springs with the following characteristics are selected to realize the prototype:

## 7. Actuators design

The parameters known so far, derived from previous calculations (wing transverse stiffness and springs stiffness), chosen on the basis of practical considerations (maximum wire load) or depending on the material availability (wire diameter), are summarised in Table 3.

The structural load/displacement ratio, evaluated from the previous F.E. analyses at the position corresponding to the second actuator, is close to 2.13 N/mm, but since this actuator is required to contribute only to the structural stiffness and not to the profile displacement (the 2<sup>nd</sup> wire load opposes just the 2<sup>nd</sup> spring load), the  $K'$  parameter in this case is set to zero.

Now it is possible to solve Eq. (8) retrieving the required wire length  $l$ , the required pre-strain displacement  $\Delta l_0$ , the equilibrium elongation in the martensitic state  $\Delta l_M$  and the equilibrium elongation

Table 2 Actuator springs parameters

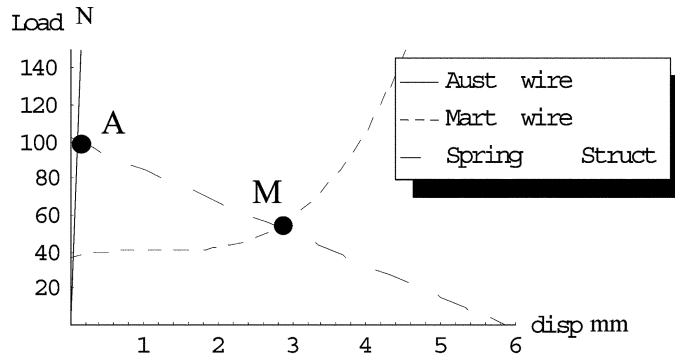
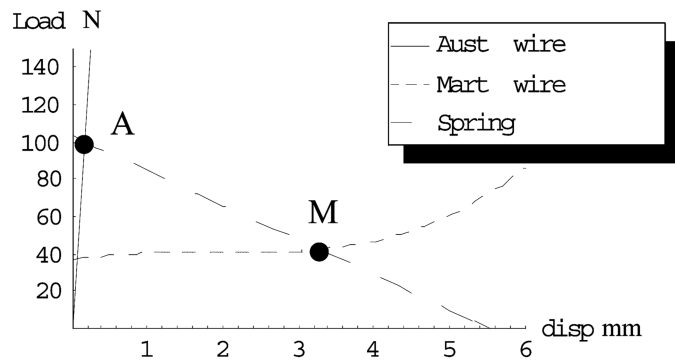
	Spring # 1	Spring # 2
Wire diameter [mm]	2	2.8
Coil diameter [mm]	16	17.2
n. of spires	5.5	7.5
Stiffness [N/mm]	11.4	18.6

Table 3 Fixed parameters for the actuator-structure model

	$d$ [mm]	$K'$ [N/mm]	$K$ [N/mm]	$F_{Amax}$ [N]
1 <sup>st</sup> Act.	1.25	5.96	11.4	100
2 <sup>nd</sup> Act.	1.25	-	18.6	100

Table 4 Parameters from solutions of Eq. (8)

	$l$ [mm]	$\Delta l_0$ [mm]	$\Delta l_M$ [mm]	$\Delta l_A$ [mm]
1 <sup>st</sup> Act.	92.7	5.9	2.8	0.1
2 <sup>nd</sup> Act.	150.9	5.6	3.3	0.2

Fig. 17 Operating chart of 1<sup>st</sup> actuatorFig. 18 Operating chart of 2<sup>nd</sup> actuator

in the austenitic state  $\Delta l_A$ .

Figs. 17 and 18 show the operating charts of the two actuators, whose parameters, summarised in Table 4, are derived by solving Eq. (8) with the  $\sigma_M(\varepsilon)$  law referred to a room temperature of 25 °C.

The abscissae  $\Delta l$  in Figs. 17 and 18 represent the wires elongation, the curves indicating the Austenitic and Martensitic response of SMA are derived by transforming the stress-strain material curves, at 120 and 25 °C respectively, into displacements and loads by using the wires cross section and minimum undeformed lengths, and the elastic response curve of the wing structure coupled to the spring is defined by the product of the stiffness  $K+K'$  by the contraction  $\Delta l - \Delta l_0$ ;

When the wires temperature is set to 25 °C, the equilibrium configurations are those visualized by points M; increasing the temperature, the corresponding configurations of each actuator are represented by points sliding upward within the segments AM, until the SMA is in its fully austenitic phase and the points A designate the corresponding working condition in the charts.

The limit load of 100 N implies that a maximum stress of about 82 MPa is achieved in the wires; then the fully austenitic phase in our actuators can be obtained with temperatures lower than 40 °C, in fact, Fig. 12 shows that at this temperature, the stress-induced martensite appears only for stress values greater than 150 MPa.

## 8. Adaptive airfoil prototype tests

The realized prototype, shown in Figs. 19 and 20, is actuated by feeding the SMA wires with different direct current–voltage values; a 4 Ampère current produced a temperature increase of 47 °C and the desired displacements after more than 2 minutes heating, 5.8 A resulted in a temperature increase of about 100 °C and in the complete profile displacement in a time of about 30 seconds, the voltage being 0.88 V and 1.41 V for the first and the second actuator respectively.

The profile shapes corresponding to the unactuated and the actuated wing, photographed in Fig. 21, are analysed by means of the “Image Pro Plus 2.0” software for image analysis, in order to measure the coordinates of many profile points to be successively compared to the reference airfoils E328 and E329.

This comparison is reported in Fig. 22, where the achievement of an acceptable degree of accuracy in the airfoil change is visible. Furthermore, it is worth noting that a considerable part of the discrepancy is

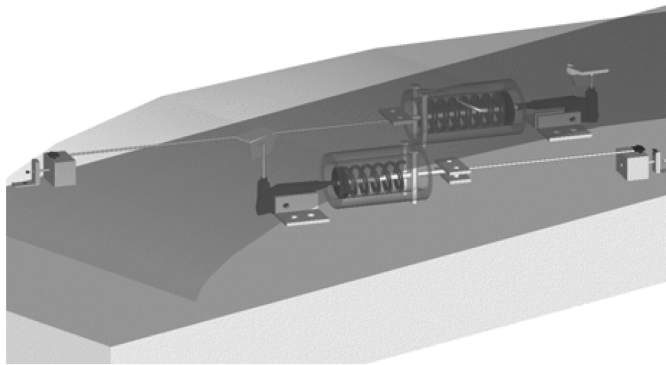


Fig. 19 Detail of the adaptive wing lay out

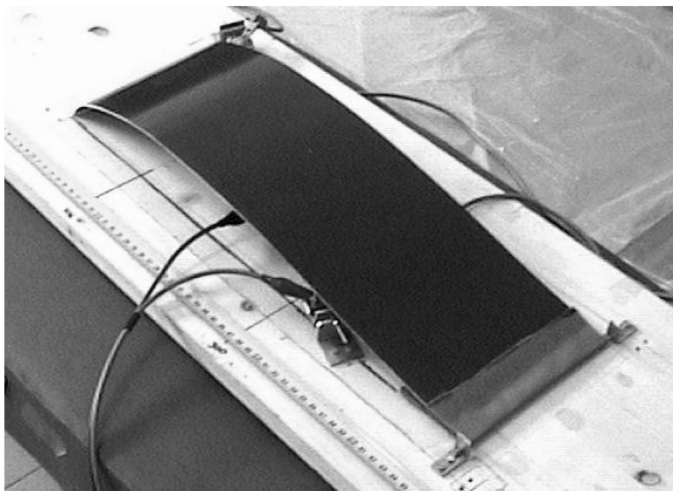


Fig. 20 Adaptive wing section prototype

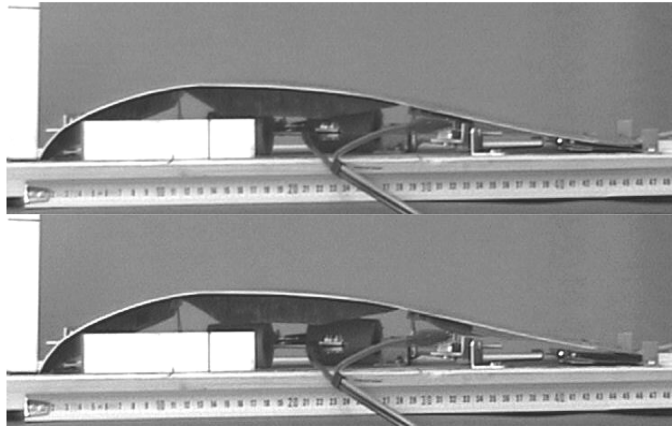


Fig. 21 Unactuated and actuated prototype shapes

due to the initial shaping of the E328 airfoil, in fact, the wood ribs over which the steel foil is glued do not copy exactly the desired initial E328 shape.

The maximum offset distance between points of the E328 airfoil and of the actuated profile is found 260 mm behind the leading edge and is equal to 1.4 mm; the distance between the same two points in the unactuated and E328 profile is 0.8 mm.

The wood ribs have a much greater flexural stiffness than the steel skin, so the profiles transformation may be regarded as a composition of rotations and translations imposed to rigid parts of the profiles, elastically joined with each other in the points where the actuators are placed: this implies that, given the number of actuated joints, the maximum possible accuracy is obtained when the actuated points of the profiles are correctly displaced so that they lie on the target airfoil, but, also in this case, the profile points at intermediate positions between two successive joints will never lie exactly on the right target profile. Clearly this cause of error can be reduced by increasing the number of joints, but the complete coincidence with the desired target profile is virtually possible only with an infinite number of joints or, more properly, with a continuously deforming rib-skin structure. Given the number of actuated joints

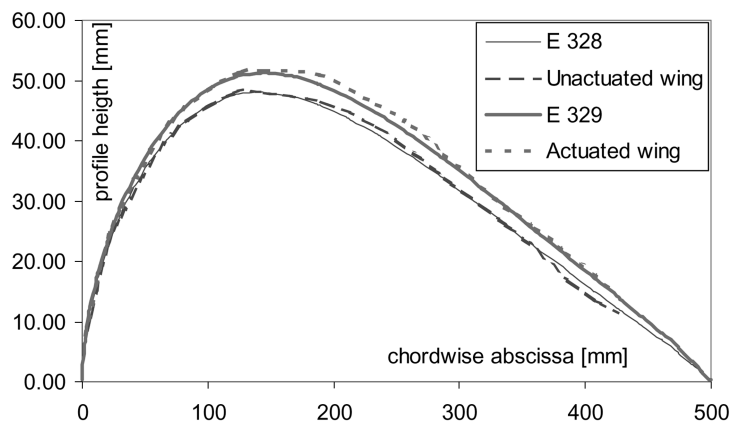


Fig. 22 Comparison between theoretical airfoils and prototype profiles

used for this application, the accuracy obtained in the reproduction of the desired profiles of Fig. 22 is considered satisfactory.

## 9. Hingeless wing lay out

The approach adopted for the design of the hingeless control surface is simpler than that used for the adaptive airfoil, because now the position of the actuating loads is almost fixed in terms of application point and vector direction.

Two couples of NiTi wires, respectively placed above and below the aileron midplane as in Fig. 23, are used to alternatively pull upward or downward the trailing edge;

the aileron is composed by a mid-plane steel plate which constitutes the main structural component, and by the surrounding aerodynamic profile realised with a cellulose sheet 0.3 mm thick. The steel plate acts as a cantilever beam connected to the remaining part of the wing on the aileron root.

The connection between the external surface and the internal steel plate is realized by rigidly joining them next to the trailing edge (on the steel wedges which also hold one endpoint of each SMA wire), and by interposing two hinged rods approximately halfway between the trailing edge and the root of the control surface. The free ends of the aileron skin are allowed to slide under the wing airfoil in the overlapping region close to the root, because, if they were fixed to the wing structure, a huge skin stretching and contraction would have been required in order to allow meaningful deflections of the aileron.

The hinged rods, made of the same cellulose sheet used for the airfoil, are needed to support the skin while allowing it to slide and to vary the airfoil thickness during the aileron deflection.

When a couple of SMA wires is heated, it induces a compressive/flexural load on the cantilever steel plate, whose elastic reaction equilibrates the tensile load of the contracting wires. The structure stiffness is due almost exclusively to the steel plate, because the bending stiffness of the cellulosic skin and the tensile stiffness of the cellulosic rods are negligible in comparison to the former.

Then the parameters to be varied in order to achieve the desired aileron deflection are those related to the SMA wires (diameter, length,  $\Delta l_M$ ,  $\Delta l_A$ ), and the dimensions of the steel plate.

The considered hingeless wing specimen has the same dimensions of that previously used for the adaptive airfoil (500 mm chord, 150 mm spanwise width), and the chord portion over which the hingeless aileron concept is applied is 100 mm long. The aileron steel plate is rectangular and its width is the same of the remaining part of the wing. Then, the only variable parameter for the steel plate is the

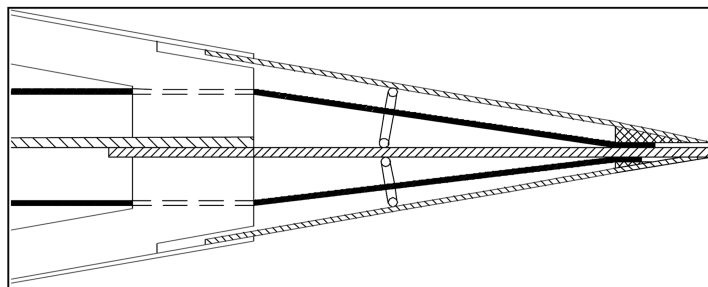


Fig. 23 Schematic section of the hingeless control surface

thickness, whose value has to be chosen according to the SMA wires performance in order to result in an acceptable aileron deflection.

It is worth noting that the length variability required to the NiTi wires in their phase transformations is almost twice that required to simply deflect the aileron in one direction starting from the undeflected or “neutral” position; in fact, when a couple of wires is cold and the antagonist couple of wires is heated starting from the neutral configuration of the aileron, the cold wires have to elongate producing as low as possible reactions and without undergoing permanent deformations.

## 10. Identification of loads and strain requirements for SMA

The coupling of the steel plate with the wires results in a highly non-linear structure which undergoes large displacements (comparable to the cantilever plate length) and significant compressive stress which could induce buckling of the structure; the response of the wires-plate system is then evaluated by analysing finite elements models such that in Fig. 24, where the plate thickness is varied among the values of 0.3 and 0.7 mm. The NiTi wires are modeled as inextensible cables because of the difficulties in modeling by F.E. the temperature-dependent stress-strain curves of the SMA and the consequent mechanical behaviour.

Simple a posteriori considerations allow to translate the results from the described F.E. analyses into design parameters for the SMA wires, in fact, the displacement imposed to the free ends of the inextensible cables in order to appropriately deform the plate are equal to the contraction required to the real NiTi wires; this data, together with the knowledge of the cable load corresponding to the above displacement, allows to calculate the required length and contraction of the wires as well as the

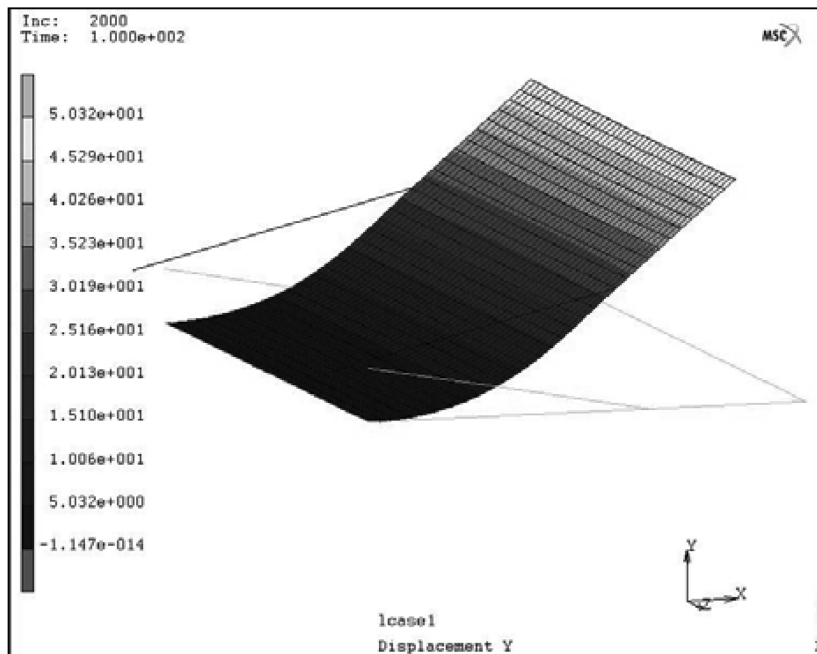


Fig. 24 F.E. model of the aileron structure

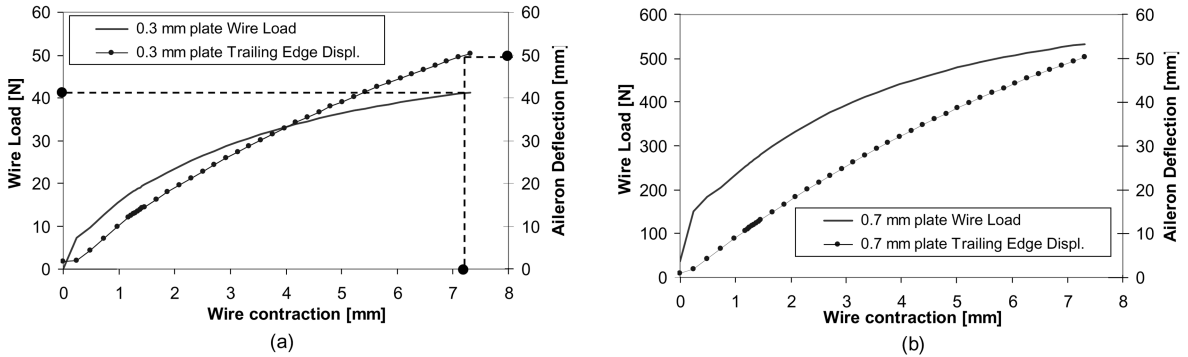


Fig. 25 Aileron deflection and wire load against wire contraction

equilibrium configurations of the wires-plate structure.

A preliminary set of F.E. analyses demonstrated that, if the wires were placed parallel to the plate, the aileron deflection would have been due just to the plate buckling and to unpredictable snap-through phenomenon which would affect the aileron deflected shape; the successive structure lay out and F.E. models incorporate a 10 degs. angle between wires and plate, so that a component of the wires traction induces bending moment on the plate and prevents the occurrence of buckling.

In these F.E. analyses is not taken into account the reaction force of the unactivated cold wires which have to elongate in order to comply with the aileron deflection, but their contribution to the resisting force which opposes the hot wires contraction is taken into account only successively in the wires-related calculations.

Fig. 25 reports the results of major interest from the F.E. analyses, expressed as the vertical displacement of the trailing edge and the tensile load of the wire, against the displacement of the cable free end (wire contraction)

The 0.3 mm thick plate is selected for the prototype development because, in the other case, the load required to satisfactorily deflect the aileron is more than ten times greater and is not compatible with the available NiTi wire sections.

For the 0.3 mm thick plate deflected by 50 mm, the contraction of the wire and its tensile load are evidenced as dark points in Fig. 25(a), while the maximum equivalent stress on the plate is 45 MPa.

## 11. Prediction of the hingeless wing behavior

The main consideration to be made in order to calculate the wires length regards their required elongation  $2\Delta l_0 = 14.6$  mm (twice that needed for a full deflection starting from the neutral position), which must correspond to a wire strain not exceeding 5% in order to be recovered with a certain safety margin by mean of the shape memory effect.

This means to choose wires whose length is 290 mm in the austenitic phase without any applied load; the diameter of the wires adopted is 1.25 mm.

The plate reaction on the wires as a function of the wire contraction (continuous curve in Fig. 25(a)) is approximated by the best fit polynomial (9), and Table 5 summarizes the structural parameters determined so far.

Table 5 Structure response at 50 mm deflection

Half-cycle wire contraction $\Delta l$	7.3	mm
Wire length $l$	290	mm
Wire diameter $d$	1.25	mm
Max. plate reaction on the wire $R(\Delta l)$	41	N

$$R(x) = 0.1944 \cdot x^3 - 2.9782 \cdot x^2 + 17.21 \cdot x \quad (9)$$

Given these data, in order to completely predict the structural response to the activation of the structure is then necessary to calculate the  $\Delta l_A$  and  $\Delta l_M$  elongations at the end of the heating and cooling phases respectively, according to the following equations

$$\begin{aligned} \sigma_A \left( \frac{\Delta l_A}{l} \right) \cdot \frac{\pi}{4} \cdot d^2 &= R(\Delta l_0 - \Delta l_A) + \sigma_M \left( \frac{2\Delta l_0 - \Delta l_A}{l} \right) \cdot \frac{\pi}{4} \cdot d^2; \\ \sigma_M \left( \frac{\Delta l_M}{l} \right) \cdot \frac{\pi}{4} \cdot d^2 &= R(\Delta l_0 - \Delta l_M); \\ \Delta l_0 &= \Delta l_A + \Delta l \end{aligned} \quad (10)$$

Eq. (10) states respectively the equilibrium of the active wires at the end of the heating process (resisting force due to reactions of the bending plate and of the passively elongating antagonist martensitic wires), the equilibrium of the active wires at the end of the cooling process (resisting force is only due to the plate reaction), and the achievement of the required variability in the wire length in an half cycle deflection.

In order to keep as low as possible the resisting force of the unactivated martensitic wires which are stretched by the activated ones, the imposed room temperature is 15 °C.

Solution of Eq. (10) gives  $\Delta l_A = 0.23$  mm,  $\Delta l_M = 5.36$  mm and  $\Delta l_0 = 7.53$  mm, corresponding to the system response shown in Fig. 26, where  $Disp(C) = \Delta l_A$ ,  $Disp(E) = \Delta l_M$ ,  $Disp(A) = \Delta l_0$ .

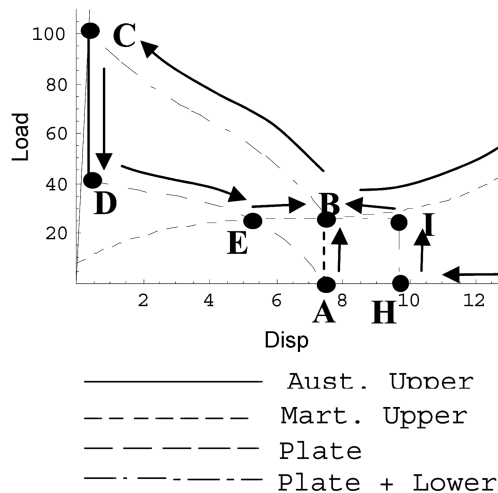


Fig. 26 Aileron response to upper wires transformations

Fig. 26 evidences that two different loading paths must be considered for predicting how the structure behaves during the heating and cooling phases of a couple of wires.

Let's suppose that, starting from the neutral position of the aileron (point **A**, upper and lower wires unloaded and cold), the upper couple of wires is heated: the first infinitesimal fraction of their shrinkage induces tensile stress in all the wires (point **B**), then the temperature and load of the upper wires continues to increase as their length decreases up to the point **C**; at the same time the lower wires, passive, cold, are forced to elongate up to point **F**; this configuration corresponds to the maximum upward deflection of the aileron; in the just concluded **B-C** load path, the force opposing the contraction of the upper wires is given by the plate elastic reaction (Eq. 9) plus the resisting load of the martensitic lower wires which behave as prescribed in the **B-F** segment of their load-displacement curve.

Then the upper wires are cooled and start to elongate; the very first infinitesimal fraction of their elongation unloads both themselves (point **D**) and the lower cold wires (point **G**), so that in the successive greater part of the upper wires cooling, the only force which tends to elongate them is due to the plate elastic reaction only. The equilibrium between the completely cooled martensitic upper wires and the plate reaction corresponds to point **E**, while the lower wires are remaining in the state of point **G** (hanging loose in their seat); this indicates that the neutral position of the aileron cannot be restored by simply interrupting the electric current which feeds the activated wires. In fact, whatever the stress values are in the martensitic upper wires and in the plate at their equilibrium point **E**, these stresses induces a residual bending of the plate.

Now the lower wires are heated and their initial contraction goes along without being opposed by any resistance until the point **H** is reached, where their "looseness" (clearance between them and the supporting structure) is recovered.

The residual elongation of lower wires at point **H** is equal to the residual contraction of the upper wires which are not yet varying their state and are remaining at the equilibrium point **E** (the curve segments **EB** and **BH** have equal projections on the abscissae axis).

The successive infinitesimal contraction of the lower wires generates tensile stress in them (point **I**) and still do not affect the upper wires; further heating induces lower wire contraction as well as upper wires elongation, until upper and lower wires reach the common state defined by point **B**.

If now the electric current in the lower wires is interrupted, all the wires relax themselves until the point **A** is reached, this configuration corresponding to the undeflected and load-free aileron structure.

If, on the contrary, the heating of the lower wires is continued, a downward deflection of the aileron is performed with a sequence symmetrical to that just described, in which the role of upper and lower wires is reversed.

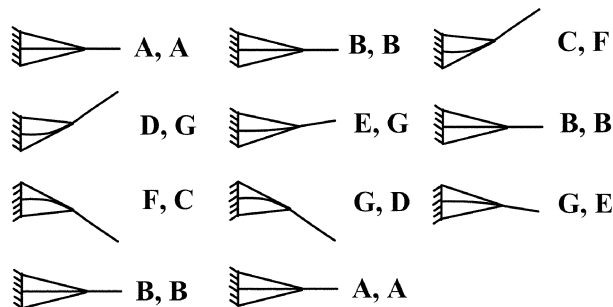


Fig. 27 Wires state sequence for an activation cycle of the aileron

A schematic sequence of a complete cyclic upward and downward deflection is shown in Fig. 27, where the first and second letter of each configuration correspond to the state of the upper and lower wires, respectively.

## 12. Prototype construction and testing

A demonstrator is realised according to the described layout and to the calculated values of the structural parameters such as the wire length, wire diameter, constraints positions, plate thickness, cantilever length. The initial assembling configuration is that of the undeflected aileron, obtained by pre-straining all the wires, at 15 °C room temperature, of the quantity  $\Delta L_0$  before locking them in place by way of screw-tightened cable heads and clamps.

The wires extremities clamped on the trailing edge are in contact with the steel plate which constitutes the backbone of the aileron, so that electrical connection among them is ensured, while the other extremities, placed in proximity of the half-chord point, are electrically insulated from each other; in this way it is possible to feed the desired sequence of wires in a series circuit by simply connecting a power supply to the half-chord extremities of the desired wires.

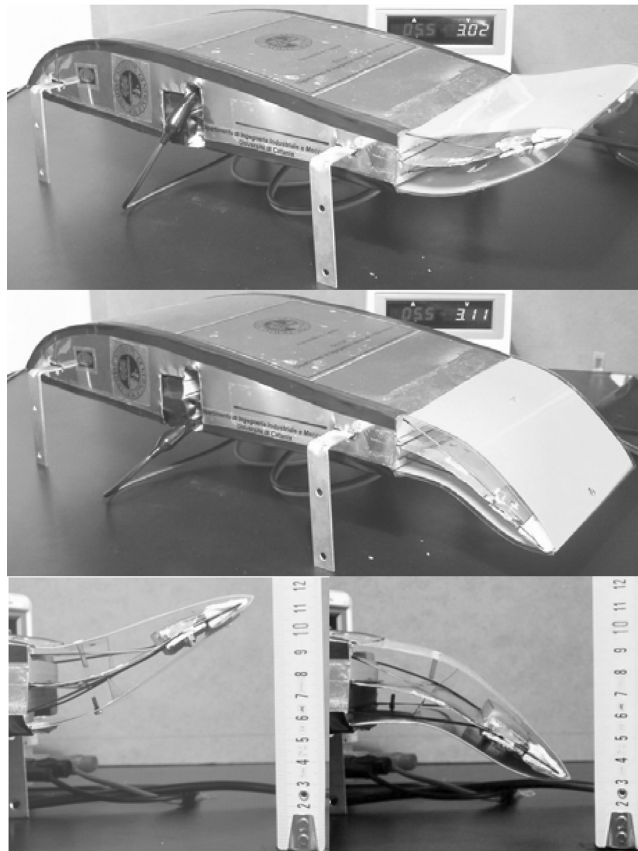


Fig. 28 Activated hingeless wing model

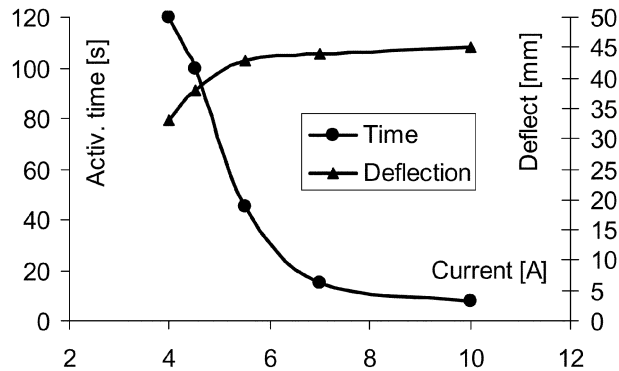


Fig. 29 Results from experimental tests on the hingeless wing

The experimental tests are performed by activating a couple of wires in turn, resulting in the deflection visible in Fig. 28.

Different activation current values are used, giving the responses summarized in Fig. 29.

An activation current of 3.5 A does not produce any aileron deflection after a 3 minutes waiting time; from this evidence and from the data in Fig. 29 it is possible to conclude that the minimum activation current lies somewhere between 3.5 and 4 A.

Given the maximum stress on the aileron structure close to 100 MPa (Fig. 26), Fig. 12 shows that the minimum activation temperature (that for which the fully austenitic phase extends up to 100 MPa) is higher than 25 °C (at this temperature the full austenitic phase exists only for stress values up to 30 MPa) and lower than 40 °C (now the fully austenitic phase exists for stress values up to 170 MPa).

An excessively long transitory time is required to activate the aileron with the minimum possible current, thus the minimum activation current could be used just to maintain the deformation once it is obtained with higher currents in more reasonable transitory times.

The upward and downward displacements of the leading edge measured for D.C. values above 5.5 A are almost stabilized on 43 mm, 14% lower than those predicted; this presumably happens because the real pre-elongation of the wires, performed before assembling them into the demonstrator, slightly differs from the one calculated by Eq. (10).

The transitory time needed before the deformed shape is assumed varies considerably with the wires activation current (Fig. 29), ranging from 120 seconds for a 4 A current to 8 seconds for the 10 A current.

The time needed for a couple of wires to return in their fully martensitic state and elongate, is largely dependent on the cooling properties of the surrounding environment, but the activation of the antagonist wires could help by promoting the stress-induced transformation of the cooling wires into martensite.

The temperatures range of 15 °C-120 °C considered in this work, resulted by the properties of the available SMA and is suitable for UAV operating at very low altitudes; in other aeronautical applications, the thermal properties of SMAs should be tailored on different operating temperatures.

Given the large temperature variations of the air surrounding conventional airplane structures, an SMA actuator system could require also thermal insulation and other means of temperature control, other than the adjustment of the alloy thermal properties from a metallurgic point of view.

The optimization of SMA operating temperatures is also essential for energetic consideration, because the temperature control may be an energetically expensive process.

Further investigation could be carried out regarding the behaviour of the system under repeated cyclic loads, in order to assess the fatigue envelope of the SMAs and the modification of their superelastic-memory effect during the expected service life of the structure.

### **13. Conclusions**

A study about shape memory alloys controlling adaptive airfoils and hingeless wing control surfaces has been performed by way of structure modeling, numerical simulation and experimental tests.

The NiTi used for this work, available in the form of wires with different diameters, has been tested in order to determine the transition temperatures and the stress-strain relationship at various temperatures.

For the investigation on the adaptive airfoil, a set of linear elastic finite elements models of the wing profile has been preliminarily analysed in order to select the most convenient location for the SMA actuators. A further series of finite elements analyses has been carried out on the best-performing actuators distribution, simulating the effect of a specified airflow-induced pressure distribution on the wing module with differently rigid actuators.

From the results of these F.E. analyses were derived the specifications for the design of the SMA actuators.

After defining the actuator layout and modelling its behaviour, the length and the pre-elongation of the NiTi wires constituting the main component of two actuators have been calculated according to the specifications previously determined. A prototype of the actuated wing module has been tested, evaluating the actuated and inactive profile shapes by way of image analysis techniques.

The comparison of the real wing profiles with the theoretical airfoils coordinates has shown a good performance of the actuation system, which is also able to ensure a structural stiffness adequate to the considered airflow pressure load.

A combined finite elements - algebraic modelling approach is used to design the hingeless wing structure, whose behaviour is more articulate than that of the adaptive airfoil.

Large displacement-finite elements analyses are carried out on two models of the aileron structure coupled to inextensible cables. The results of these F.E. analyses have been used to choose some parameters of the aileron structure as well as the specifications to be used for the calculation of the required length and pre-elongation values of the NiTi wires.

The structural behaviour has been modeled, evidencing that after a deflection is imposed to the aileron it cannot return to its undeflected position without a further activation of some SMA wires.

A significant trailing edge displacement, close to 10% of the wing chord, is achieved in the experimental tests confirming that the force and the work developed by the SMAs is suitable for this kind of applications.

The transitory time of the NiTi phase transformation induced by Joule effect heating does not affect the performance of the adaptive airfoil because its tuning on different flight conditions is supposed to require significant rapidity; on the contrary, for the hingeless control surfaces a quick response is essential.

Different activation current values have been used to deflect the hingeless aileron, indicating that a control system able to opportunely variate the feeding current could lead to satisfactory response also in terms of deflection rapidity.

## Acknowledgements

The financial support of the NSFC Joint Research Fund for Overseas Chinese Young Scholars under 50228808 is gratefully acknowledged.

## References

- Auricchio, F. and Sacco, E. (1999), "A temperature-dependent beam for shape-memory alloys: constitutive modelling, finite-element implementation and numerical simulations", *Comput. Methods Appl. Mech. Eng.*, **174**, 171-190.
- Brinson, C. (1993), "One-dimensional constitutive behavior of shape memory alloys: thermomechanical derivation with non-constant material functions and redefined martensite internal variable", *J. Intell. Mat. Struct.*, **4**, 229-242.
- Brinson, C. L. and Huang, M. S. (1996), "Simplifications and comparisons of shape memory alloy constitutive models", *J. Intell. Mat. Struct.*, **7**, 108-114.
- Brocca, M., Brinson, L. C. and Bazant, Z. P. (2002), "Three-dimensional constitutive model for shape memory alloys based on microplane model", *J. Mech. Phys. Solids*, **50**, 1051-1077.
- Di Lecce, M. (1997), *Fondamenti di Aerotecnica*, IBN Editore, Rome.
- Drela, M. (2001), *XFOIL v6.9 User Guide*, MIT Aero & Astro Harold Youngren Aircraft, Inc.
- Ezley, D. M., Aarash, Y. N. and Wadley, H. N. G. (2005), "A shape memory based multifunctional structural actuator panel", *Int. J. Solids Struct.*, **42**, 1943-1955.
- FLemings, G. A. and Burner, A. W. (1999), "Deformation measurements of smart aerodynamic surfaces", *44<sup>th</sup> SPIE International Symposium on Optical Science, Engineering and Instrumentation*.
- Garner, L. J., Wilson, L. N., Lagoudas, D. C. and Rediniotis, O. K. (2000), "Development of a shape memory alloy actuated biomimetic vehicle", *Smart. Mat. Struct.* **9**, 673-783.
- Govindjee, S. and Garrett, J. H. (2000), "A computational model for shape memory alloys", *Int. J. Solids Struct.*, **37**, 735-760.
- Huang, W. (2002) "On the selection of shape memory alloys for actuators", *Materials and Design*, **23**, 11-19.
- Icardi, U. (2001), "Large bending actuator made with SMA contractile wires: theory, numerical simulation and experiments", *Composites Part B*, **32**, 259-267.
- Kroo, I. (1997), *Applied Aerodynamics: a Digital Textbook*, Version 4.1, Stanford, Desktop Aeronautics, Inc.
- Lu, K.-J. and Kota, S., (2002), "Compliant mechanism synthesis for shape-change applications: preliminary results", *SPIE Conference on Smart Structures and Materials*, **4693**, 161-172.
- Lu, K. Z. and Weng, G. J. (1997), "Martensitic transformations and stress-strain relations of shape-memory alloys", *J. Mech. Phys. Solids*, **45**, 1905-1928.
- Monner, H. P. (2001), "Realization of an optimized wing camber by using formvariable flap structures", *Aerosp. Sci. Technol.*, **5**, 445-455.
- Neal, D. A., Matthew, C. G. Johnston, C. O., Robertshaw, H. H., Mason, W. H. and Inman, D. J. (2004), "Design and wind-tunnel analysis of a fully adaptive aircraft configuration", *AIAA paper 2004-1727*.
- Strelec, J. K., Lagoudas, C. C., Khan, M. A. and Yen, J. (2003), "Design and implementation of a shape memory alloy actuated reconfigurable airfoil", *J. Intell. Mat. Syst. Struct.*, **14**, 257-273.
- Tanaka, K., Nishimura, F., Hayashi, T., Tobushi, H. and LExcellent, C. (1995), "Phenomenological analysis on subloops and cyclic behaviour in shape memory alloys under mechanical and/or thermal loads", *Mech. Mat.*, **19**, 281-292.
- Tanaka, K., Nishimura, F. and Tobushi, H. (1995), "Transformation start lines in TiNi and Fe-based shape memory alloys after incomplete transformations induced by mechanical and/or thermal loads", *Mechanics of Materials*, **19**, 271-280.
- Talay, T. A. (1975), "Introduction to the aerodynamics of flight", Langley Research Centre, NASA SP367.
- Trochu, F., Sacépé, N., Volkov, O. and Turenne, S. (1999), "Characterization of NiTi shape memory alloys using dual kriging interpolation", *Mater. Sci. Eng.*, **A273**, 395-399.
- Van Blyenburgh, P. (1999), "UAVs: an overview", *Air and Space Europe*, **1**, 43-47.